ACS APPLIED MATERIALS & INTERFACES

www.acsami.org Research Article

Self-Promoting Mechanism of Oxalic Acid in Ce−CN-Assisted Photocatalytic Ozonation for Water Treatment

Qi Chen, Weirui Chen,* Jing Wang, Gaozu Liao, Xukai Li, Xingmei Guo,* and Laisheng Li*

Cite This: ACS Appl. Mater. Interfaces 2025, 17, 50650−50664 Read Online

ACCESS | Metrics & More | Article Recommendations | Supporting Information

ABSTRACT: Small molecular carboxylic acids (SCAs) are common in natural waters, but their impact on advanced oxidation processes (AOPs) is understudied. This study investigates the effects of various carboxylic acids, such as oxalic acid (OA), formic acid (FA), acetic acid (AA), succinic acid (SA), and benzoic acid (BA), on a Ce single-atom-doped graphitic carbon nitride (Ce−CN) photocatalytic ozonation (PCO) system. Among the tested SCAs, only OA significantly promoted O_3 activation and pollutant degradation. When degrading atrazine (ATZ), Ce−CN performed worse than CN, but Ce−CN exhibited superior activity when OA was the target. The OA removal was 98% in the PCO/Ce−CN system, while it was 82% in the PCO/CN system in 30 min. The introduction of OA also enhanced ATZ removal from 55 to 86% within 5 min in the PCO/Ce−CN system. Moreover, OA's yield during macromolecular organic compound degradation and its proportion among SACs affected PCO/Ce−CN activity. Mechanistic studies showed that OA could bind with Ce−CN, forming a Ce−OA complex that facilitated ligand-to-metal electron transfer (LMET), reducing the redox potential of the Ce(III)/Ce(IV) cycle, enhancing the ATZ removal efficiency, and boosting ozone activation. O_3 decomposed into *O and •OH on Ce−CN, which were the primary reactive oxygen species for pollutant degradation. These findings highlighted the unique role of OA in Ce-based PCO systems, offering insights for enhancing AOP performance.

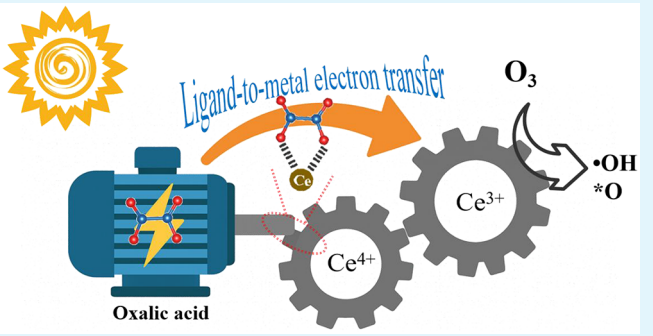

KEYWORDS: *photocatalytic ozonation, cerium-doped g-C_3N_4, oxalic acid, ligand effects, valence cycling*

1. INTRODUCTION

With the acceleration of industrialization, water pollution had become increasingly severe, which was potentially harmful to the environment.[1] Traditional water treatment methods often struggled to remove these persistent organic pollutants (POPs), making the development of new and efficient water treatment technologies particularly important.[2] Photocatalytic ozonation (PCO) technology was an emerging water treatment and had garnered widespread attention for its potential in environmental remediation.[3]

PCO combined the advantages of photocatalysis and ozonation, characterized by its high efficiency, environmental friendliness, and sustainability. The core of PCO involved the excitation of photocatalysts and activation of ozone (O_3).[4] Under light irradiation, the photocatalyst was excited to generate electron−hole pairs ($h_{vb}^+-e_{cb}^-$), and these high-energy carriers could react with water molecules, dissolve oxygen (DO), and O_3 to produce highly reactive oxygen species (ROS).[5] Under the joint function of the ROS, organic pollutants in water were oxidized, which facilitated their degradation. The development and optimization of catalysts were at the core of PCO. Researchers were dedicated to synthesize novel photocatalysts, such as g-C_3N_4,[6] metal oxides,[7] and composite materials,[8] to enhance their light absorption capacity, the separation efficiency of $h_{vb}^+-e_{cb}^-$, and reactivity with O_3. Researchers assessed the effectiveness of catalysts and explored the involved mechanism with the help of a range of organic pollutants, such as dyes,[9] pharmaceuticals,[10] and pesticides.[11] However, they primarily used deionized water as the background solution. In practical water treatment, water bodies often contained various organic pollutants and coexisting substances, such as inorganic ions, other organic compounds, and suspended solids.[12] These coexisting substances significantly affected the effectiveness of PCO.

Recently, some researchers had noted the unique function of coexisting substances on AOPs. For instance, coexisting substances, like Cl^-, might compete with a photocatalyst for O_3, thereby decreasing the amount of O_3 available for generating ROS.[13] Some organic compounds would be

Received: May 12, 2025
Revised: August 10, 2025
Accepted: August 18, 2025
Published: August 27, 2025

https://doi.org/10.1021/acsami.5c09397
ACS Appl. Mater. Interfaces 2025, 17, 50650−50664

absorbed onto the surface of the catalyst, either occupying the surface active sites[14] or hindering the separation of h_{vb}^{+}−e_{cb}^{-}.[15] Carboxy compounds, like oxalic acid (OA), benzoic acid (BA), and humic acid (HA), were special substances commonly found in actual water.[16,17] Moreover, in the PCO process, the degradation of organic pollutants would also yield these carboxy compounds. For a long time, researchers considered that the above-mentioned substances were harmful to the AOP process because they exhibited strong chelation with metal sites, which masked active centers or consumed ROS.[18] However, recently, some studies showed that certain carboxyl compounds, like OA, could promote electron transfer and enhance ROS production.[19,20] However, little attention was given to the influence of these coexisting carboxy compounds on the PCO process.

This study focused on the influence of coexisting carboxylic acids on the PCO process for treating organic pollutants, using single-atom cerium-doped g-C_3N_4 (Ce−CN). In comparison to pure g-C_3N_4 (CN), cerium doping enhanced photocatalytic properties, such as light absorption, and increased ozone reactivity. Notably, Ce−CN exhibited improved PCO activity for oxalic acid (OA) but lower activity for atrazine (ATZ) compared to CN. Ce−CN outperformed CN in ATZ degradation only in the presence of OA. Similar promoting effects were observed with humic acid (HA). To better understand the impact of small organic carboxylic acids on the PCO system, comparative experiments and characterizations, including X-ray photoelectron spectroscopy (XPS), attenuated total reflection Fourier transform infrared spectroscopy (ATR−FTIR), electron paramagnetic resonance (EPR), *in situ* Raman spectra, and electrochemical potential measurements, were conducted.

2. EXPERIMENTAL SECTION

2.1. Reagents. Atrazine (ATZ), cerium nitrate hexahydrate [$Ce(NO_3)_3{\cdot}6H_2O$, 99.5%], succinic acid (SA), and formic acid (FA) were obtained from Shanghai Macklin Biochemical Co., Ltd. Dicyandiamide, oxalic acid dihydrate (OA), and humic acid (HA) were bought from Aladdin Biochemical Technology Co., Ltd. Acetic acid (AA), NaOH, and HCl were purchased from Guangzhou Chemical Reagent Factory. Methanol, acetonitrile, and phosphoric acid were obtained from Tianjin Kemiou Chemical Reagent Co., Ltd. Benzoic acid (BA) and citric acid (CA) were bought from Tianjin Zhiyuan Chemical Reagent Co., Ltd. Agar powder was bought from Guangdong Huankai Microbial Sci. & Tech. Co., Ltd. All chemicals used in this research were at least analytically pure grade.

2.2. Synthesis of Catalysts. To synthesize the Ce−CN catalyst, 1.00 g of dicyandiamide (11.9 mmol) and 0.217 g of $Ce(NO_3)_3{\cdot}6H_2O$ (0.50 mmol) were mixed into 20 mL of deionized water. The mixed solution was then stirred for 60 min in a water bath at 60 °C and then continually stirred at 90 °C until the water was completely evaporated. Next, the remaining mixture was ground into powder and then heated at 600 °C for 3 h under a N_2 atmosphere to obtain Ce−CN.[21] g-C_3N_4 was prepared analogously to Ce−CN by dissolving 2.00 g of dicyandiamide in 20 mL of DI water and then following identical synthesis procedures.

2.3. Characterization of Materials. The physical composition, crystallinity, and structural characterization of the catalysts were studied by X-ray diffraction (XRD, Bruker D8 ADVANCE, Germany) with Cu Kα radiation. The functional groups and chemical bonds of the catalysts were studied by Fourier transform infrared (FTIR, Thermo Scientific iN 10, U.S.A.), and the scanning wavelength was 500−4000 cm^{-1}. The monatomic structure was obtained by high-angle annular dark field scanning tunneling electron microscopy (HAADF−STEM, JEM-ARM300F, Japan), and the distribution of elements on the sample surface was obtained by STEM mapping. The Ce concentrations of Ce−CN and Ce leaching were measured by inductively coupled plasma−atomic emission spectrometry (ICP−MS). The surface chemical elements and bond characteristics were investigated by X-ray photoelectron spectroscopy (XPS, Thermo Scientific K-Alpha, U.S.A.) with Al Kα radiation. The valence and coordination structure of catalysts were obtained by X-ray absorption spectroscopy (XAS), and the extended X-ray absorption fine structure spectra were processed using IFEFEIT. Wavelet transform (WT) was measured by the software package (K = 10 and σ = 1) developed by Funke and Chukalina. The absorbance of samples in the ultraviolet (UV) and visible range was measured by ultraviolet−visible diffuse reflectance spectroscopy (UV−vis DRS, Shimadzu, UV-2600, Japan). An electrochemical workstation (CHI 660E, Zhenhua, China) with 0.1 M Na_2SO_4 (electrolyte solution) was used to depict the Mott−Schottky (M−S) curves and electrochemical impedance spectroscopy (EIS). The composite rate of e_{cb}^{-} and h_{vb}^{+} was measured by photoluminescence (PL) spectra (Hitachi, F-4600, Japan) at room temperature. The Lewis acid site was detected by pyridine adsorption Fourier transform infrared spectroscopy (Py−IR, Brook, Tensor 27, Germany). The specific surface area and pore size of the samples were analyzed by a gas adsorption desorption instrument (Micromeritics ASAP 2460, U.S.A.) with the Brunauer−Emmett−Teller (BET) method. The ROS produced during the catalytic process were detected by EPR (Bruker A300, Germany), and the specific test conditions and instrument parameters were enclosed in Text S1 and Table S1 of the Supporting Information. *In situ* Raman spectra of Ce−CN in the presence and absence of ozone were taken with a confocal micro-Raman spectrometer (inVia, Renishaw) at a laser light irradiation of 633 nm and a resolution of 1 cm^{-1}.

2.4. Experimental Procedure. The PCO reaction was conducted in a double-glass cylindrical reactor with a volume of 1.4 L. O_3 was generated from dry air through an ozone generator (flow rate, 1.0 L/min; input power, 20 mg/h) and then bubbled into the reactor through an aeration plate at the bottom. A 300 W long arc xenon lamp, which was placed in a quartz tube with a bushing, was used, and its wavelength was ~310 W/m^2. The circulating cooling water was passed into the quartz tube bushing to keep the temperature of the reaction solution constant. A 0.1 g catalyst was mixed with the reaction solution, poured into the reaction column, and then sampled at the set time. All water samples were quenched with $NaHSO_3$ and filtered before analysis.

2.5. Analysis Method. The concentrations of ATZ and different carboxylic acids (except HA) were measured by HPLC (LC10A, Shimadzu, Japan). The injection volume for all samples was 100 μL, and other detailed information was presented in Table S2. The concentration of HA was measured by an ultraviolet−visible spectrophotometer (UV-5200PC), with the wavelength (λ) of 254 nm.

The synergy factor (η) represents the coupling of light exposure (P) and heterogeneous catalytic ozonation (HCO) in the PCO process [$\eta = k_{PCO}/(k_P + k_{HCO})$], which could be used to access the role of Ce in the catalyst. The reaction constants (k) were calculated by the pseudo-first-order equation (eq 1)

$$\ln(C_0/C_t) = kt \tag{1}$$

where C_0 represented the initial concentration of contaminants, C_t represented the concentration of contaminants at a certain time, and t was the reaction time.

The typical horseradish peroxidase method was adopted to measure H_2O_2 due to its low concentration in solution.[22]

The Tauc plots could be converted from the UV−vis diffuse reflectance spectra (UV−vis DRS) according to eq 2

$$(\alpha h\nu)^2 = A(h\nu - E_g) \tag{2}$$

where α, h, ν, A, and E_g correspond to the absorbance coefficient, Planck constant, light frequency, constant, and bandgap energy, respectively.[23,24]

https://doi.org/10.1021/acsami.5c09397
ACS Appl. Mater. Interfaces 2025, 17, 50650−50664

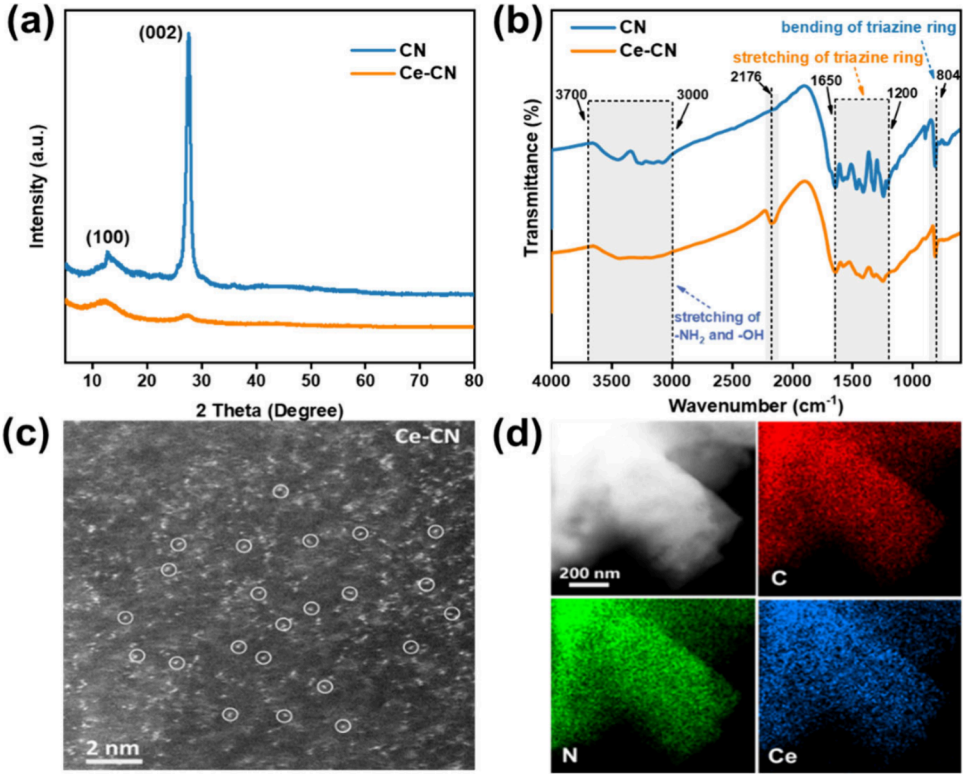

Figure 1. (a) XRD pattern and (b) FTIR spectra of CN and Ce−CN, (c) HAADF−STEM image, and (d) elemental mapping image of Ce−CN.

The conduction band (CB) position (vs Ag/AgCl, pH 7) could be converted into the CB position (vs NHE, pH 7) according to the conversion equation (eq 3).[25]

$$E_{NHE} = E_{Ag/AgCl} - 0.197 + 0.059pH \quad (3)$$

The valence band (VB) position could be obtained via eq 4.

$$E_{VB} = E_{CB} + E_g \quad (4)$$

The R_{CT} value, which was defined as the ratio of •OH exposure to O_3 exposure, could be obtained by measuring the concentrations of O_3 and the •OH probe compound (*p*-CBA)[26] (eq 5)

$$R_{CT} = \frac{C_{\bullet OH}}{C_{O_3}} = \frac{\ln\left(\frac{C_{p\text{-CBA},t}}{C_{p\text{-CBA},0}}\right)}{-k_{\bullet OH,p\text{-CBA}}} \frac{1}{\int C_{O_3,t}\,dt} \quad (5)$$

where $C_{p\text{-CBA},0}$ was the initial concentration of *p*-CBA, $C_{p\text{-CBA},t}$ and $C_{O_3,t}$ were the concentrations of *p*-CBA and O_3 at a certain time, and $k_{\bullet OH,p\text{-CBA}}$ (5×10^9 M^{-1} s^{-1}) was the secondary rate constant, which represented the reactivity between •OH and *p*-CBA. The O_3 concentration could be measured by the indigo method (Text S2), and $\ln(\frac{C_{p\text{-CBA},t}}{C_{p\text{-CBA},0}}) = \ln(\frac{R_{CT}O_{3,t}}{R_{CT}O_{3,0}}) = \ln(\frac{O_{3,t}}{O_{3,0}})$. Equation 6 was obtained by fitting the curve of the O_3 concentration with time. Thus, the R_{CT} value could be evaluated only by analyzing the O_3 concentration.

$$C_{O_3,t} = a - be^{ct} \quad (6)$$

The electrode potential (φ) of Ce−CN with different ligands was estimated by the electromotive forces (E) of constructed reversible cells, which were measured by a compensation method using a digital potential difference measuring instrument (SDC, Nanjing Sangli Electronic Equipment Factory). The reversible cells were shown in eq 7, with the calomel electrode (saturated KCl solution) as the cathode and an aqueous solution mixed with Ce−CN powder as the anode. The method of making a salt bridge is shown in Text S3. The temperature throughout the experiment was 25 °C. The conditional potential of the calomel electrode could be estimated by eq 8 (vs SHE) to avoid the effect of the temperature. The cathode potential of Ce−CN with different carboxylic acid ligands at different concentrations was obtained by eq 9.[27]

$$Hg_{(l)}|Hg_2Cl_{2(s)}|KCl||Ce{-}CN\ solution|Pt_{(s)} \quad (7)$$

$$\varphi_{calomel} = 0.2412 - 6.61 \times 10^{-4}(T - 25) - 1.75 \times 10^{-6}(T - 25)^2 - 9.16 \times 10^{-10}(T - 25)^3 \quad (8)$$

$$\varphi_{Ce-CN} = E + \varphi_{calomel} \quad (9)$$

3. RESULTS AND DISCUSSION

3.1. Textural Properties of Catalysts. Crystal structures of CN and Ce−CN were examined using XRD. As depicted in Figure 1a, both samples exhibited two signals at $2\theta = 13.1°$ and 27.6°, matching JCPDS 87-1526.[24] The peak at 13.1° corresponded to the (100) plane, associating with the repeating units of *s*-triazine, whereas the peak at 27.6° corresponded to the (002) plane, which reflected the stacking of the aromatic structure.[28] The intensity of the peaks in Ce−CN was significantly lower compared to that of pure CN, suggesting a reduction in crystallinity due to perturbations of the stacked layers.[19,29] Furthermore, no peaks corresponding to cerium oxides were detected, indicating that the Ce atoms were effectively distributed and successfully incorporated into the CN skeleton.[6,19]

As demonstrated in Figure 1b, all absorption peaks of CN could be observed in the FTIR pattern of Ce−CN, demonstrating that Ce doping did not alter the structure of CN. The band at 804 cm^{-1} corresponded to the bending mode of the *s*-triazine ring, while bands in the range of 1200−1650 cm^{-1} were related to the stretching vibrations.[24] The weak

https://doi.org/10.1021/acsami.5c09397
ACS Appl. Mater. Interfaces 2025, 17, 50650−50664

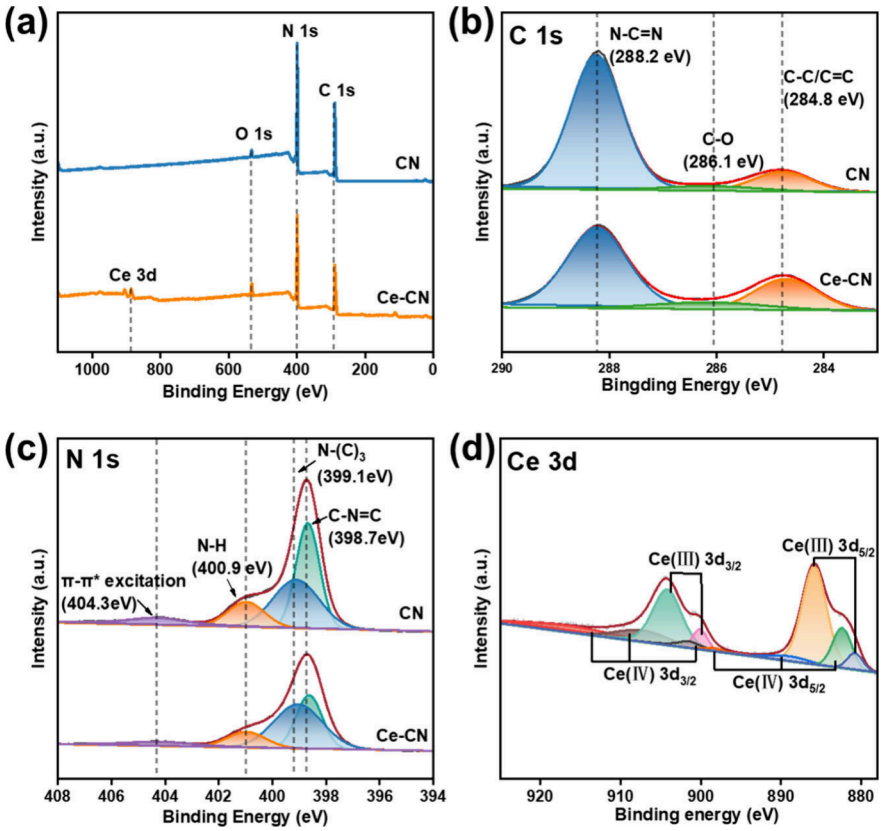

Figure 2. (a) XPS survey spectra of CN and Ce−CN and (b) C 1s spectra, (c) N 1s spectra, and (d) Ce 3d spectra of Ce−CN.

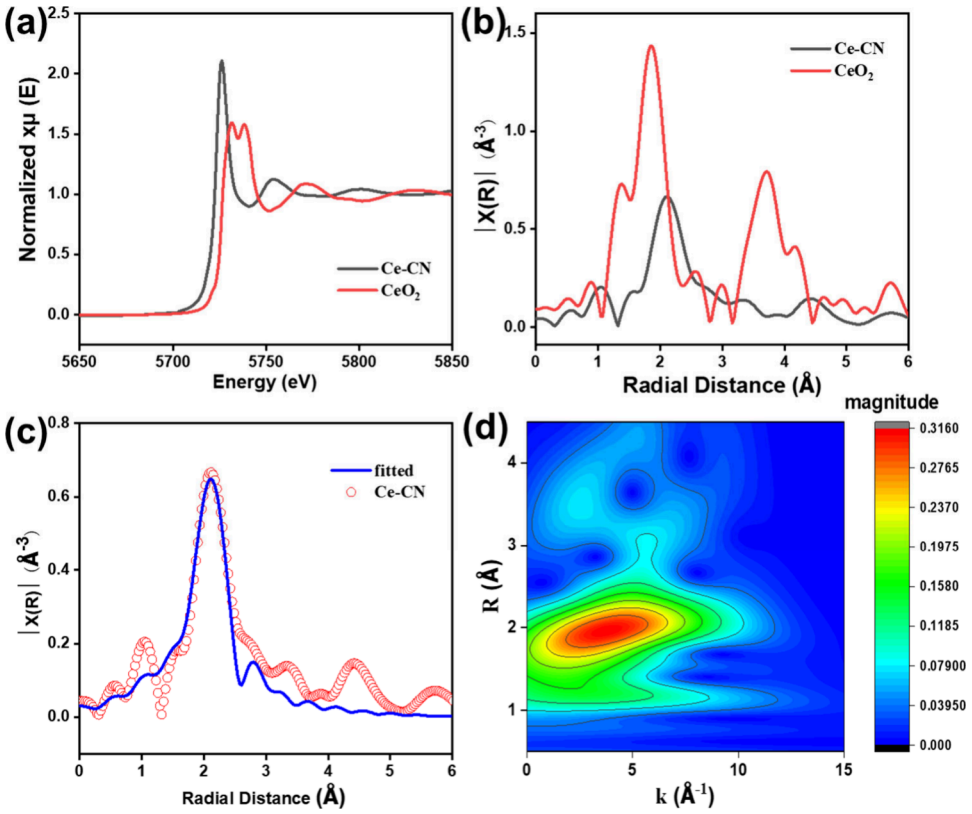

Figure 3. (a) Ce L-edge XANES spectra, (b) Ce L-edge FT-EXAFS spectra, (c) EXAFS fitting curves at *R* space, and (d) WTs for the k^3-weighted EXAFS signals of Ce−CN.

https://doi.org/10.1021/acsami.5c09397
ACS Appl. Mater. Interfaces 2025, 17, 50650−50664

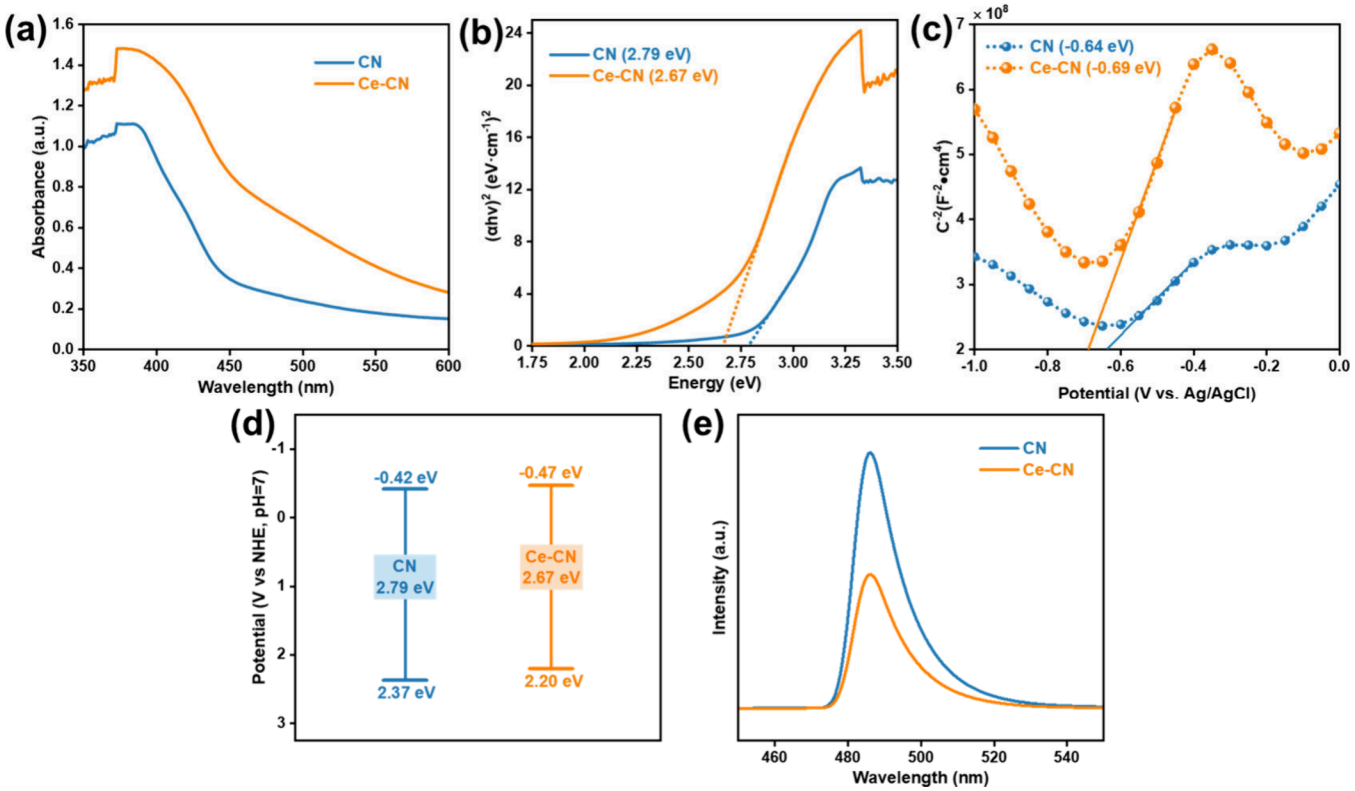

Figure 4. (a) UV−vis DRS spectra, (b) Tauc plots, (c) M−S plots, (d) band structure, and (e) PL spectra.

band at 2176 cm^{-1} was attributed to surface defects associated with the −C≡N bond, which was induced by the presence of Ce ions.[30] The broad bands between 3000 and 3700 cm^{-1} corresponded to N−H stretching vibrations from NH_2/NH groups and O−H bonds from absorbed H_2O.[19] CeO_2, typically produced during the preparation of Ce-containing catalysts, showed characteristic peaks near 624 and 3400 cm^{-1}.[19,31] However, no such peaks were detected in the Ce−CN sample, further confirming the successful Ce doping, which was consistent with XRD results. Ce doping weakened the peak intensities of CN, likely due to the formation of Ce−N−C bonds, disrupting the *s*-triazine ring structure. Notably, no peaks for the Ce−N bond were observed in the FTIR spectrum because of the low Ce content in the Ce−CN sample. ICP−MS measurement indicated that the Ce content in Ce−CN was only 11.33 atom %, with a maximum leaching of 0.05 atom % during a 30 min PCO process, demonstrating the stability of Ce−CN during the reaction. N_2 adsorption−desorption isotherms of both CN and Ce−CN were classified as type III. S_{BET} values for CN and Ce−CN were found to be 24.42 and 12.15 m^2/g, respectively (Figure S1 and Table S3). To investigate the distribution of Ce atoms in Ce−CN, HAADF−STEM was performed. As demonstrated in Figure 1c, bright spots representing Ce atoms were clearly observed throughout the CN matrix, with no aggregation detected.[32] Elemental mapping (Figure 1d) further confirmed the uniform distribution of C, N, and Ce atoms on the CN nanosheets.

As displayed in the full spectrum (Figure 2a) of XPS, C, N, O, and Ce elements could be detected in Ce−CN, among which the peak of O 1s mainly came from surface-absorbed CO_2 and H_2O.[23] The C 1s spectrum of both samples (Figure 2b) could be fitted into three peaks at 284.8, 286.1, and 288.2 eV, corresponding to amorphous C (C−C/C═C), surface-adsorbed H_2O (C−O), and the sp^2 hybridization of *s*-triazine units (N−C═N), respectively.[6] The N 1s spectrum (Figure 2c) was divided into four peaks. The peak at 398.7 eV was attributed to sp^2-hybridized nitrogen (C═N−C),[33] which confirmed the presence of sp^2-bonded CN. Other peaks at 399.1, 400.9, and 404.3 eV were indexed as bridged N [N−$(C)_3$], N−H bond, and $\pi-\pi^*$ excitation between stacked layers, respectively.[6] As shown in Figure 2d, the spectrum of Ce 3d could be spit into 10 peaks. The peaks at 900.1 and 904.2 eV corresponded to ≡Ce(III) of Ce $3d_{3/2}$, while the peaks at 901.5, 907.3, and 916.7 eV were attributed to ≡Ce(IV) of Ce $3d_{3/2}$. The peaks located at 880.8 and 885.9 eV were ≡Ce(III) of Ce $3d_{5/2}$, while the peaks at 882.4, 889.0, and 898.4 eV were indexed as ≡Ce(IV) of Ce $3d_{5/2}$, which indicated the existence of Ce(IV)/Ce(III) redox pairs.[34]

XAS was employed to further explore the chemical environment of Ce in Ce−CN. As demonstrated in the X-ray absorption near-edge structure (XANES; Figure 3a), the absorption threshold of Ce−CN was smaller than that of CeO_2, indicating that the average valence state of the Ce atom in Ce−CN was less than +4, suggesting that Ce−CN contained both Ce(III) and Ce(IV), which was consistent with the result of XPS. The Fourier transform extended X-ray absorption fine structure (FT-EXAFS) (Figure 3b) demonstrated that the peaks of the Ce atom in Ce−CN were distinct from those of Ce−Ce and Ce−O bonds in CeO_2, proving that CeO_2 did not exist in Ce−CN and Ce existed in the form of a single atom, which was in agreement with the result of HAADF−STEM. The EXAFS in *R* space and the corresponding fitting curve were shown in Figure 3c, and the corresponding fitted data were shown in Table S4. The coordination number of Ce with N atoms was 4 ± 0.3, forming a Ce−N coordination structure with an average Ce−N bond

https://doi.org/10.1021/acsami.5c09397
ACS Appl. Mater. Interfaces 2025, 17, 50650−50664

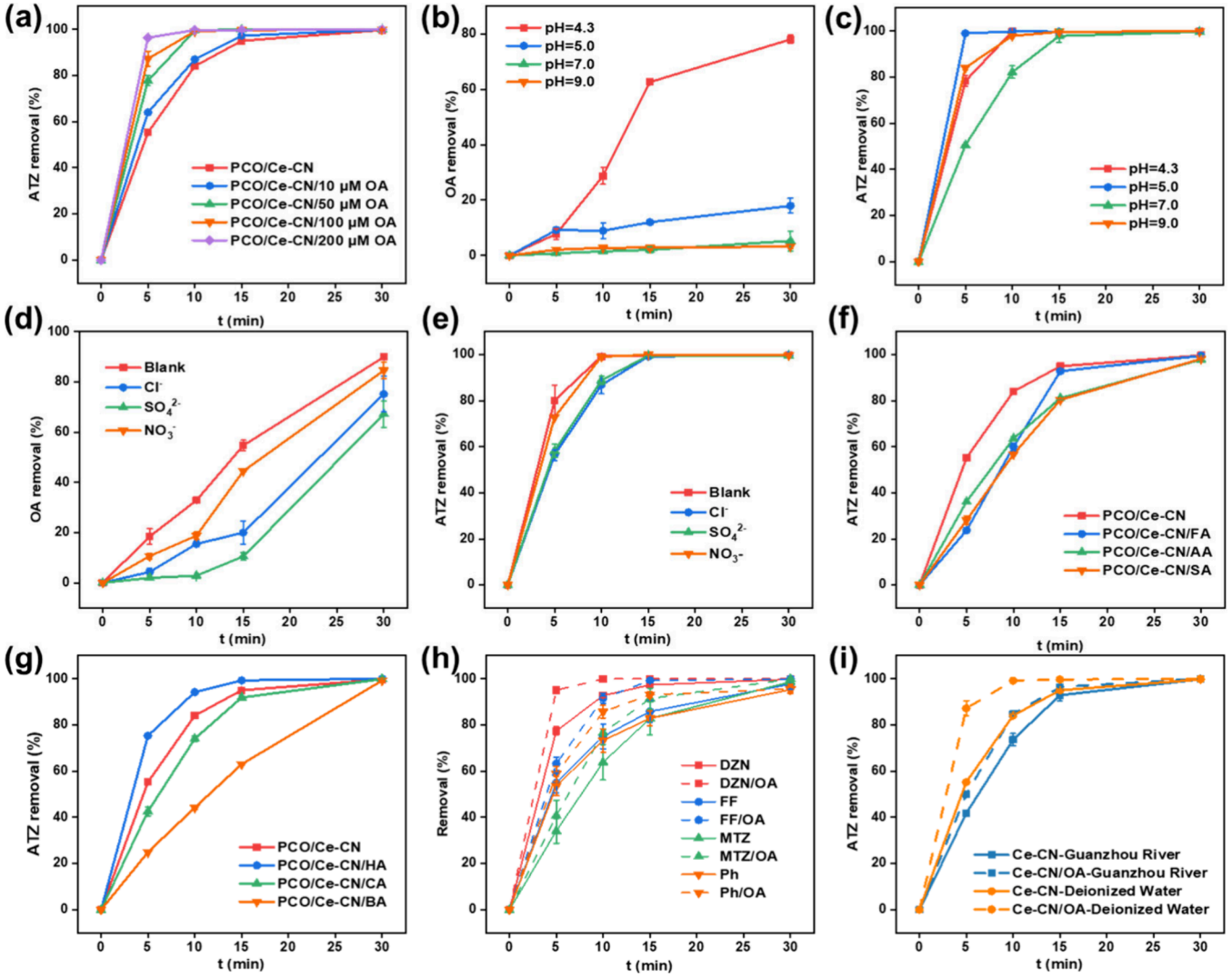

Figure 5. Influence of (a) different OA concentrations, (b and c) initial pH, and (d and e) common anions (2 mM) in the dual-pollutant system, influence of (f) other small carboxylic acids and (g) other macromolecular carboxylic acids on ATZ removal, (h) degradation of typical pollutants, and (i) ATZ removal in real water. Reaction parameters: dosage of catalyst, 0.1 g/L; concentrations of carboxylic acids, 100 μM; concentrations of pollutants, 10 μM; volume, 1 L; and temperature, 25 °C.

length of 2.61 Å. To elucidate the atomic-scale structure of the catalyst, density functional theory (DFT) calculations were performed. As shown in Figure S2, the optimized Ce−CN configuration revealed four coordinated Ce−N bonds with an average bond length of 2.62 Å. This theoretical value showed excellent agreement with experimental characterization data (Table S5), exhibiting merely a 0.4% deviation, which validates the reliability of the model. WT (Figure 3d) further confirmed the coordination of Ce−CN, and the maximum intensity occurred at about 3 $Å^{-1}$, corresponding to the Ce−N bond. All the above outcomes demonstrated the incorporation of Ce atoms into CN in the form of Ce−N bonds. The single-atom structure of Ce−CN not only enhanced atomic utilization efficiency but also provided a unique structure that facilitates in-depth investigation of catalytic mechanisms.

3.2. Optical and Electronic Properties of Catalysts. UV−vis DRS (Figure 4a) showed that both Ce−CN and CN exhibited absorption around 380 nm, which was attributed to electronic transitions between N 2p and C 2p orbitals.[35] Ce doping caused a red shift in CN's absorption edge and enhanced its response in the UV and visible light regions, suggesting the superior photocatalytic activity for Ce−CN.[23] The bandgap energies (E_g) of Ce−CN and CN were 2.67 and 2.79 eV, respectively, indicating that Ce doping could narrow the bandgap, reduce the minimum energy required to generate electron−hole pairs from absorbed photons, thus enhance optical absorption, and increase the generation of $h_{vb}^{+}-e_{cb}^{-}$ (Figure 4b). M−S plots in Figure 4c confirmed that both CN and Ce−CN were n-type semiconductors, and their CB positions were determined as −0.42 and −0.47 eV (vs NHE, pH 7) (eq 3). Correspondingly, their VB positions were calculated as 2.37 and 2.20 eV (Figure 4d and eq 4). Furthermore, both CN and Ce−CN exhibited fluorescence emission peaks near 485 nm in the PL pattern (Figure 4e), but the fluorescence intensity of Ce−CN was weaker than that of CN, indicating a lower recombination rate of $h_{vb}^{+}-e_{cb}^{-}$ due to Ce doping.

In summary, Ce doping enhanced the light-harvesting ability, charge transfer rate, and $h_{vb}^{+}-e_{cb}^{-}$ separation efficiency of pure CN, which strengthened the photocatalytic performance.

https://doi.org/10.1021/acsami.5c09397
ACS Appl. Mater. Interfaces 2025, 17, 50650−50664

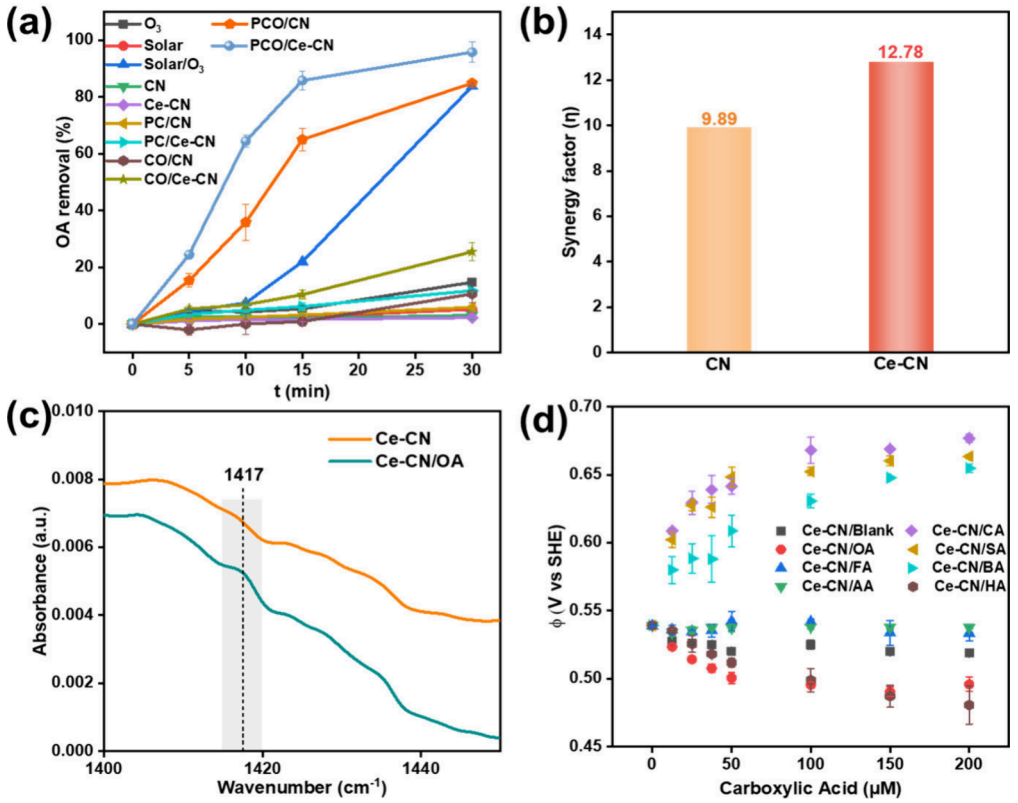

Figure 6. (a) Comparison of OA degradation in different systems, (b) synergy factor (η) of CN and Ce−CN, (c) ATR−FTIR spectra, and (d) redox potential of Ce(III)/Ce(IV) in different systems. Reaction parameters: dosage of catalyst, 0.1 g/L; OA concentration, 100 μM; volume, 1 L; and temperature, 25 °C.

3.3. Photocatalytic Ozonation Performance. ATZ was initially used as a model pollutant to investigate the PCO activity of Ce−CN. As shown in Figure S3a, surprisingly, the ATZ removal in the PCO/Ce−CN process was lower than that in the PCO/CN process. The removal of ATZ by the PCO/CN process was close to 100% within 10 min, while it was only 84% by the PCO/Ce−CN process. According to the previous characterization results, the incorporation of Ce into the CN framework could markedly improve charge separation, and the recombination of h_{vb}^{+}−e_{cb}^{-} was effectively suppressed. However, Ce−CN showed lower activity than CN, which could be ascribed to the change of ROS generation affected by Ce species. Normally, there existed one-, two-, and three-electron reductions of O_3 during the PCO process (eqs 10−12).[21] As shown in Figure S3b, a greater amount of H_2O_2 was generated in the PCO/Ce−CN process over that of the PCO/CN process, which suggested that more e_{cb}^{-} was used to reduced DO into H_2O_2, which then activated O_3 into ROS, which hindered the one-electron pathway (eq 12).

$$O_2 \xrightarrow{e^-} {}^{\bullet}O_2^- \xrightarrow{e^-} HO_2^{\bullet}/H_2O_2 \xrightarrow{O_3} {}^{\bullet}OH \quad (10)$$

$$O_2 \xrightarrow{e^-} {}^{\bullet}O_2^- \xrightarrow{e^-} HO_2^{\bullet}/H_2O_2 \xrightarrow{e^-} {}^{\bullet}OH \quad (11)$$

$$O_3 \xrightarrow{e^-} {}^{\bullet}O_3^-/HO_2^{\bullet} \rightarrow {}^{\bullet}OH \quad \text{or} \quad O_2 \xrightarrow{e^-} {}^{\bullet}O_2^- \xrightarrow{O_3} {}^{\bullet}OH \quad (12)$$

However, when OA and ATZ coexisted (Figure S3c) in the PCO/CN process, ATZ removal was inhibited. Only 86% ATZ was removed in 10 min by the PCO/CN process. However, in the PCO/Ce−CN process, it was interesting to see that the addition of OA increased ATZ removal. ATZ degradation reached almost 100% in 10 min. As for OA removal (Figure S3d), the degradation rate of OA in the PCO/Ce−CN system (89.9%) was greater than that in the PCO/CN system (52.8%). OA was highly stable, which was inert to O_3 (k_{OA,O_3} = 0.039 M^{-1} s^{-1}) and h_{vb}^{+}, but it could be attacked by $^{\bullet}OH$ ($k_{OA,^{\bullet}OH}$ = 7.7 × 10^6 M^{-1} s^{-1}).[36] Generally, OA should compete with ATZ for ROS, which was expected to hinder the degradation of ATZ, as observed in the PCO/CN process. The enhancement in the PCO/Ce−CN process reflected the change in the mechanism.

To further investigate the role of OA, the influence of the OA concentration on ATZ degradation was considered (Figure 5a). As the OA amount rose from 10 to 200 μM, ATZ removal gradually increased. Notably, when the OA concentration reached 200 μM, ATZ removal achieved 100% within just 5 min. Similarly, OA removal in the dual-pollutant system also increased with higher initial concentrations of OA (Figure S4). These results further suggested that, in the PCO/Ce−CN system, OA enhanced the generation of ROS through its own degradation rather than competing with ATZ for ROS. The influence of pH on the performance of the PCO/Ce−CN process was systematically explored with OA and ATZ as dual pollutants. As demonstrated in Figure 5b, OA removal efficiency significantly reduced with solution pH, which suggested that acidic conditions were more favorable for the generation of ROS in the PCO/Ce−CN system. As shown in eqs 13 and 14, H^+ was vital to the production of $^{\bullet}OH$ in the PCO process. Under alkaline conditions, the hydroxide ions (OH^-) accelerated the decomposition of O_3, thereby weakened the synergistic effect between photocatalysis and

https://doi.org/10.1021/acsami.5c09397
ACS Appl. Mater. Interfaces 2025, 17, 50650−50664

ozonation.[37] At pH 9, OA removal in the PCO/Ce−CN system was approximately equal to the combined removal rates of the standalone ozonation and photocatalytic systems.

$$O_3 + e^- + H^+ \rightarrow {}^{\bullet}OH + O_2 \quad (13)$$

$$O_2 + 3e^- + 3H^+ \rightarrow {}^{\bullet}OH + H_2O \quad (14)$$

As depicted in Figure 5c, ATZ degradation in the dual-pollutant system was highest at pH 5. This was because, as the pH increased from 4.3 to 5.0, OA was gradually deprotonated from $HC_2O_4^-$ to $C_2O_4^{2-}$, which was more conducive to the generation of the Ce−OA complex. However, with a further increase in pH, Ce(III) underwent hydroxylation with OH^-, forming $Ce(OH)^{2+}$ and $Ce(OH)_2^+$. These hydroxylated species exhibited a low affinity for $C_2O_4^{2-}$, thereby reducing the production of the active Ce−OA complex.[27] The influences of various anions were also explored (Figure 5d and e). The presence of NO_3^- inhibited the degradation of both OA and ATZ, whereas SO_4^{2-} and Cl^- had a more pronounced inhibitory effect, which was due to the scavenging of $^{\bullet}OH$.[38]

In addition to OA, the effects of other common carboxylic acids found in natural environments, such as FA, AA, and SA, were also investigated (Figure 5f). However, these carboxylic acids all exhibited an inhibitory effect on ATZ degradation. The unique role of OA could be attributed to its enhanced coordination capability, stronger electronic influence, greater lowering of the Ce(III)/Ce(IV) redox potential, and unique binding configuration (see section 3.4.1). Considering that the degradation of large organic compounds might generate SCAs, humic acid (HA), citric acid (CA), and benzoic acid (BA) were also introduced into the system (Figure 5g). Interestingly, among these, only HA demonstrated a promoting effect on the PCO/Ce−CN system for ATZ degradation. The adsorption of HA on Ce−CN led to a decrease in the electrode potential of Ce−CN, attributable to HA's strong electron-donating capability, which enhanced the reducing capacity of Ce(III) (Figure 6d). Additionally, the types of small carboxylic acids produced during the breakdown of larger carboxylic acids also accounted for these differences. As shown in Figure S5a, the degradation of HA, CA, and BA was accompanied by the production of OA and FA, while only limited amounts of AA and SA were detected. HA degradation yielded the highest OA concentration at 63 μM, along with 95 μM FA. In comparison, CA degradation produced the lowest OA production at 20 μM and a slightly higher FA level of 104 μM. Meanwhile, BA degradation resulted in OA production at 45 μM and the highest FA accumulation at 220 μM. Experiments were further conducted to demonstrate the facilitation effect of OA. As demonstrated in Figure S5b, compared to the existence of 100 μM FA, the addition of 50 μM OA promoted the degradation of ATZ. The above results suggested that the co-function of OA and HA on the PCO/Ce−CN system was dependent on OA produced. In addition to the unique role of *in situ* generated OA, the enhancement induced by HA can be attributed to its ability to lower the redox potential of the Ce(III)/Ce(IV) couple (shown in section 3.4.1). This potential reduction is particularly significant as it facilitates the Ce^{3+}/Ce^{4+} redox cycling, which serves as a critical factor for efficient ozone activation.[27]

To further explore the promoting effect of OA on the Ce−CN system, we evaluated the degradation efficiency of other pollutants. As shown in Figure 5h, the removal rates of diazinon (DZN), florfenicol (FF), metronidazole (MTZ), and phenol (Ph) significantly increased with the addition of OA. Additionally, when using water samples from the Guanzhou River (Guangzhou City, Guangdong Province, China) as the reaction medium (water quality parameters were detailed in Table S6), though the overall PCO efficiency was lower than that in deionized water, the introduction of OA also enhanced the ATZ removal (Figure 5i). Generally, common water constituents, including HCO_3^-, Cl^-, and organic natural organic matter (NOM) components, could inhibit the degradation process by scavenging $^{\bullet}OH$.[39] Moreover, NOM could also compete for Ce sites with OA, thereby reducing the PCO activity. The three-dimensional excitation−emission matrix (3DEEM) fluorescence spectra were employed to study the inference of water components in the Guanzhou River on the Ce−OA interaction. As demonstrated in Figure S6a and b, a pronounced quenching effect in the aromatic compound region (particularly for tyrosine-like fluorophores) was observed following Ce−CN exposure, indicating substantial adsorption of these natural organic matter components from river water.[40] This observation was corroborated by ATR−FTIR spectroscopic analysis (Figure S6c), which revealed characteristic vibrational bands in the 1010−1300 cm^{-1} range (attributable to aromatic C−O/C−N stretching modes) exclusively present in the river-water-treated Ce−CN samples. Therefore, it was reasonable to infer that the aromatic moieties competitively occupied the Ce sites, leading to the partial deactivation of the catalytic surface. However, the addition of OA markedly improved the removal rate of ATZ in river water. These findings emphasized the unique role of OA in the PCO/Ce−CN system and its potential to enhance the water treatment efficiency in real-world applications.

3.4. Mechanism Exploration. *3.4.1. PCO/Ce−CN Activity for OA.* To further elucidate the role of OA, the comparative OA removal in the PCO process was studied. As shown in Figure 6a, systems like O_3, solar, CN, PC/CN, and CO/CN exhibited minimal OA degradation (less than 25%), indicating their limited oxidative activity. Moderate OA removal efficiencies were observed for CO/Ce−CN, with removal rates remaining below 40% after 30 min. The PCO/CN system exhibited notable OA removal, reaching approximately 85%. Among all systems, the PCO/Ce−CN system demonstrated the highest OA removal efficiency, achieving nearly 100% removal within 30 min. The synergy coefficient of PCO/CN and PCO/Ce−CN processes was calculated as 9.89 and 12.78, respectively (Figure 6b and Table S7), which reflected that the degradation of OA was a synergistic effect of photocatalysis and ozonation, and the greater catalytic activity and synergetic effect were obtained by Ce−CN.

As a matter of fact, Ce doping introduced redox-active Ce^{3+}/Ce^{4+} centers, which enhanced electron transfer and facilitated the continuous generation of ROS. Under the influence of O_3, Ce^{3+} was oxidized to Ce^{4+}, which was subsequently reduced by e_{cb}^-. This Ce^{3+}/Ce^{4+} redox cycle ensured sustained catalytic activity and consistent ROS production throughout the reaction process.[41,42] OA, as a weak organic acid, had the ability to chelate metal ions, including those of Ce and other metals involved in the AOP system.[19,43] This chelation could stabilize the Ce^{3+} ion and facilitate the redox cycling between Ce^{3+} and Ce^{4+}, which could continuously generate ROS (such as $^{\bullet}OH$ and $O_2^{\bullet -}$) to enhance the degradation of contaminants.[27] However, it should be noted that other tested carboxylic acids, like FA, AA, and SA, did not accelerate the

https://doi.org/10.1021/acsami.5c09397
ACS Appl. Mater. Interfaces 2025, 17, 50650−50664

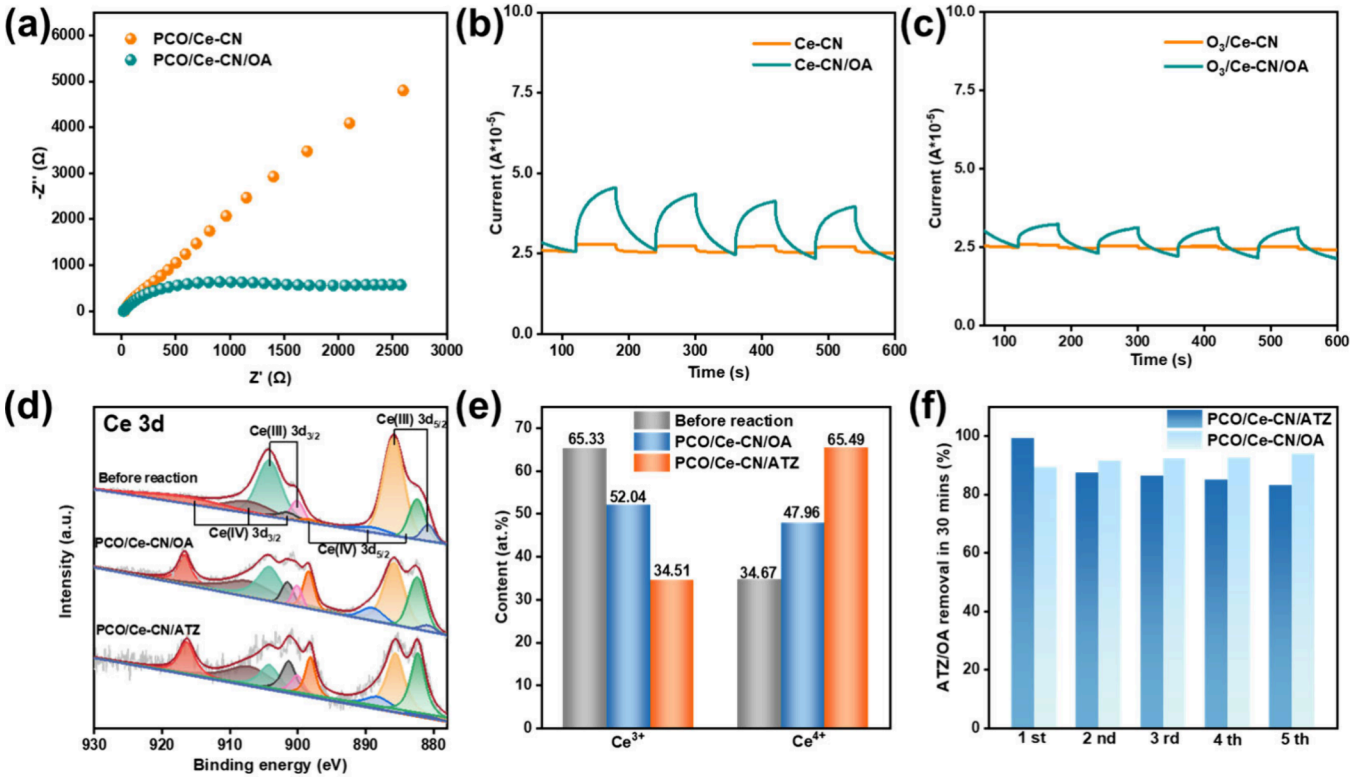

Figure 7. (a) EIS plots and (b and c) photocurrent curves of Ce−CN and Ce−CN/OA, (d) XPS and (e) valence bar chart of Ce, and (f) cyclic tests of Ce−CN for ATZ and OA degradation.

PCO activity of Ce−CN, though they could also chelate with Ce sites. The unique function of OA could be attributed to its greater coordination capability, stronger electronic influence, greater lowering of the Ce(III)/Ce(IV) redox potential, and unique binding configuration.[27] To further verify the above proposal, ART−FTIR, DFT calculation, and CV tests were conducted.

DFT calculations were carried out to explore the chelation of selected carboxylic acids with Ce−CN. Considering that all adsorption models share g-C_3N_4 as a base and that carboxylic acid and Ce active centers are actually responsible for the interactions, the DFT model can be simplified to focus on the interaction between carboxylic acids and the Ce active center to enhance computational efficiency. As shown in Table S8, the adsorption of OA on Ce sites exhibited the greatest adsorption energy, which reflected the greater coordination capability of OA. Moreover, compared to other molecules, OA binds to Ce(III) in a side-on bidentate coordination mode, whereas other molecules adopt an end-on bidentate configuration (Figure S7). The side-on coordination mode is more conducive to electron delocalization between the metal and ligand, thereby enhancing catalytic activity.[44] ATR−FTIR was employed to investigate the interaction of OA with Ce−CN (Figure 6c). The C═O stretching band of OA, normally located at 1400 cm^{-1}, was shifted to 1417 cm^{-1} when OA and Ce−CN coexisted, indicating that OA coordinated with the Ce active sites. This interaction resulted in the formation of the OA−Ce coordination complex, thereby modifying the chemical environment and electronic structure of the catalyst, which were expected to enhance electron transfer and promote ROS generation, contributing to improved catalytic performance.[37] Furthermore, OA also demonstrates a pronounced electron-donating effect, substantially increasing the charge on the Ce(III) center (Figure S8). This electronic effect enhances the capability of electron transfer from Ce(III) to O_3, thereby promoting the activation and decomposition of O_3.

To highlight the role of OA in facilitating the ligand-to-metal electron transfer, the effects of different carboxylic acids on the electrode potential (φ, measured in volts vs SHE) of Ce−CN complexes were also systematically compared. φ values exhibited a concentration-dependent trend, with variations observed depending on the type of carboxylic acid. As shown in Figure 6d, for FA, AA, CA, SA, and BA, φ values generally increased with rising concentrations and their overall values were consistently higher than those of OA and HA. The Ce−CN/OA complex displayed the lowest electrode potential across all concentrations, with a significant reduction even at low concentrations (~50 μM). This behavior aligned with the strong electron-donating ability of OA, which enhanced the reduction capacity of Ce(III). The pronounced decrease in φ observed for Ce−CN/OA underscored OA's ability to effectively shift the redox potential of the Ce(III)/Ce(IV) couple, thereby making the Ce(III)−OA complex more reactive toward O_3. Therefore, it was evident that OA was significantly more effective in modulating the redox potential of Ce(III)/Ce(IV).

3.4.2. Influence of OA on Interfacial Electron Behavior. Our previous study demonstrated that the metal component in g-C_3N_4 could accept e_{cb}^-, thereby enhancing interfacial electron transfer.[6] As shown in Figure S9a, the EIS radius of Ce−CN was significantly smaller than that of CN, demonstrating its superior electron transport capability. Ce−CN exhibited a notably lower photocurrent than CN under illumination, suggesting that e_{cb}^- were preferentially captured by Ce before participating in O_3 activation (Figure S9b and c). Upon the addition of OA, the EIS radius of PCO/Ce−CN was further

https://doi.org/10.1021/acsami.5c09397
ACS Appl. Mater. Interfaces 2025, 17, 50650−50664

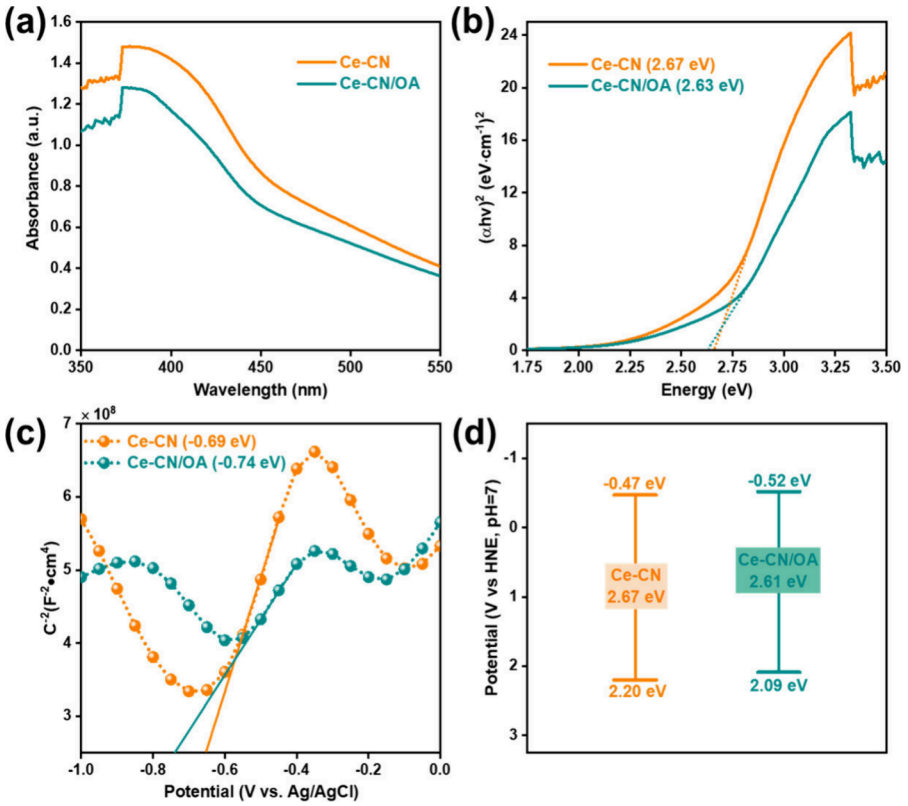

Figure 8. (a) UV−vis DRS spectra, (b) Tauc plots, (c) M−S plots, and (d) band structures of Ce−CN and Ce−CN/OA.

reduced (Figure 7a), while the photocurrents of both PC/Ce−CN and PCO/Ce−CN increased, indicating that OA facilitated interfacial electron migration (Figure 7b and c).

According to the reported literature, OA could form complexes with metal active centers, and the resulting metal−oxalate complexes may facilitate the valence state cycling of active metals.[27] To verify this hypothesis, the valence state changes of Ce by using XPS under different systems were examined. As shown in Figure 7d and e, Ce primarily existed in the trivalent (Ce^{3+}) and tetravalent (Ce^{4+}) states in Ce−CN. Fresh Ce−CN contained 65% Ce^{3+} and 35% Ce^{4+}. After PCO/Ce−CN treatment of ATZ, the Ce^{3+} proportion significantly decreased to 34%, indicating that Ce−CN lost electrons during the O_3 activation. The rate of reduction of Ce^{4+} to Ce^{3+} was relatively slow, leading to the accumulation of high-valence Ce species. However, after PCO/Ce−CN treatment in the presence of OA, the Ce^{3+} content only decreased to 52%, demonstrating that OA enhanced the ability of Ce active centers to store e_{cb}^-, thereby promoting the valence state cycling of Ce.

The valence state of the metal was strongly related to its catalytic activity. As shown in Figure 7f, when ATZ was solely treated, the PCO activity of Ce−CN gradually decreased over 5 cycles. In contrast, when OA was targeted, the catalytic activity of Ce−CN remained largely unchanged. This finding further confirmed that OA promoted the valence state cycling of Ce, which favored for its catalytic activity.

3.4.3. Influence of OA on Optical Properties of Ce−CN. UV−vis DRS showed a slightly lower absorbance for Ce−CN/OA compared to Ce−CN, with a slight reduction in the bandgap from 2.67 to 2.63 eV (Figure 8a and b). This indicated the enhanced electronic interactions between the Ce center and OA, which facilitated electron excitation and improve redox activity. The CB potential shifted downward from −0.47 eV for Ce−CN to −0.52 eV for Ce−CN/OA, while the VB potential decreased slightly from 2.20 to 2.09 eV (Figure 8c and d). The downward shift in both CB and VB indicated that OA enhanced the electronic structure of Ce−CN, promoting an improved electron transfer process. The increased CB potential of Ce−CN induced by OA highlighted its ability to activate the oxygen complex of O_3. These findings demonstrated that OA effectively tailored the optical, electronic, and electrochemical properties of Ce−CN during the PCO reaction. By promotion of electron transfer and reduction of the bandgap, OA significantly enhanced the catalytic performance of Ce−CN, establishing it as a promising candidate for redox-driven and PCO applications.

3.4.4. Generation of ROS. EPR was conduted to explore the production of ROS. As shown in Figure 9a and b, $^{\bullet}OH$ and $^{\bullet}O_2^-$ were detected, with DMPO−$^{\bullet}OH$ exhibiting a characteristic quartet (1:2:2:1 pattern), while DMPO−O_2^- displayed a sextet. The concentrations of these ROS varied significantly under different conditions. The $^{\bullet}OH$ level in PCO/Ce−CN showed only a little enhancement when compared to that in PCO/CN. However, after the introduction of OA, the generation of $^{\bullet}OH$ in the Ce−CN/PCO system significantly increased. As for $^{\bullet}O_2^-$, in the PCO system, these radicals were primarily generated from the reaction between e_{cb}^- and dissolved oxygen ($O_2 + e^- \rightarrow {}^{\bullet}O_2^-$). The $^{\bullet}O_2^-$ concentration in the PCO/CN system was markedly greater than that in the PCO/Ce−CN system. This discrepancy could be attributed to the competition between Ce and O_2 for e_{cb}^-. Following the addition of OA, the concentration of $^{\bullet}O_2^-$ in the PCO/CN system was unchanged, while the concentration in the PCO/Ce−CN system significantly decreased. This suggested that Ce−OA complexes could more effectively consume e_{cb}^-.

https://doi.org/10.1021/acsami.5c09397
ACS Appl. Mater. Interfaces 2025, 17, 50650−50664

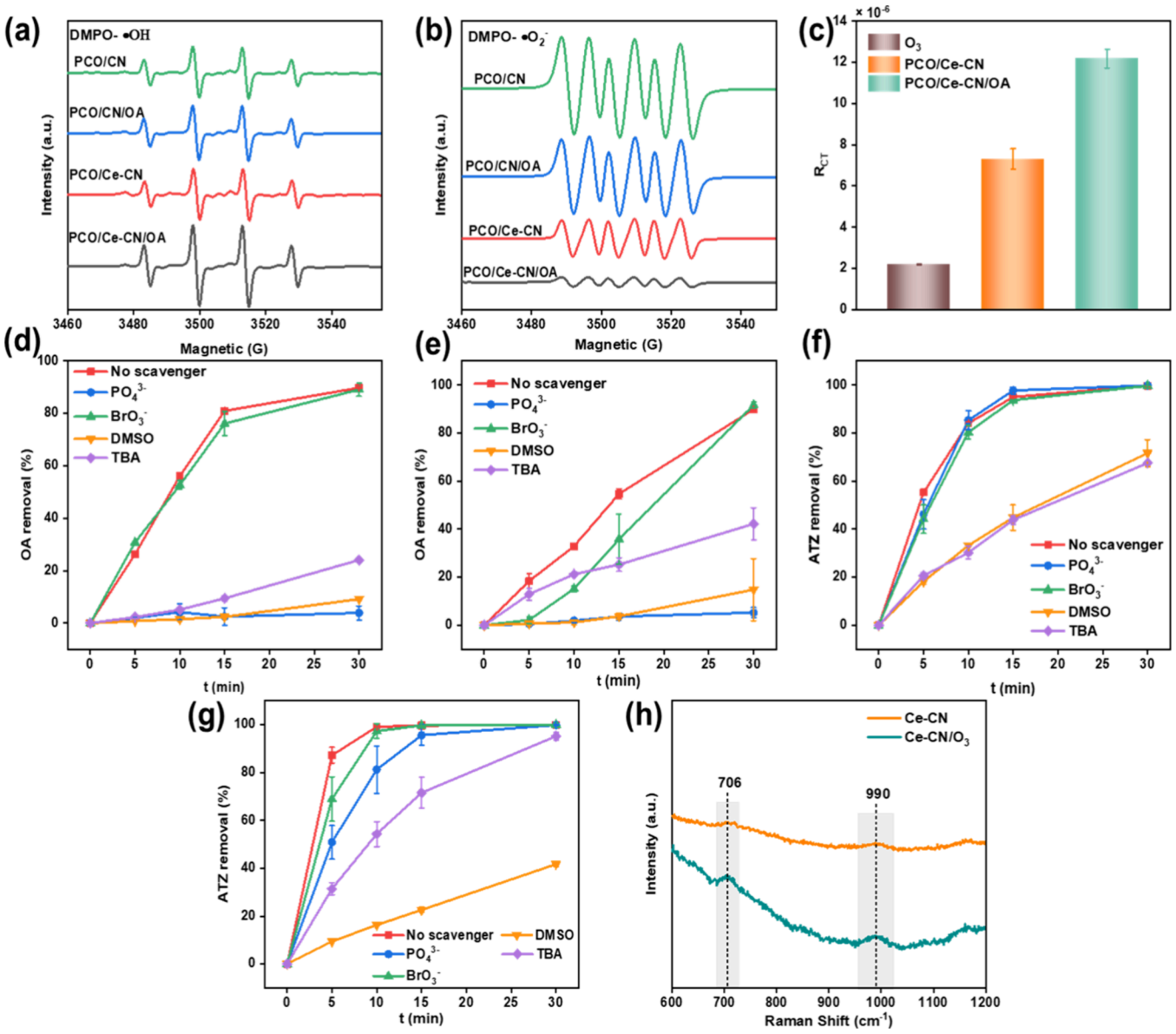

Figure 9. EPR pattern of (a) DMPO−•OH and (b) DMPO−$^{\bullet}O_2^-$, (c) R_{CT} values in different systems, influence of scavengers on OA or ATZ removal in (d and f) single-pollutant and (e and g) dual-pollutant systems, and (h) *in situ* Raman spectroscopy. Reaction parameters: dosage of catalyst, 0.1 g/L; ATZ concentration, 10 μM; concentration of scavengers, 100 μM; volume, 1 L; and temperature, 25 °C.

The R_{ct} value was utilized to assess the proportion of •OH exposure in different systems, and the relevant parameters were detailed in Figure S10 and Table S9. As demonstrated in Figure 9c, the addition of OA further increased the exposure of Ce−CN to •OH, indicating a greater •OH generating rate in the PCO/Ce−CN/OA system. The contribution of ROS to pollutant degradation was explored by adding scavengers. BrO_3^-, TBA, and DMSO were used to quench e_{cb}^-, free •OH, and surface ROS (including *•O and *•OH). PO_4^{3-} was also introduced to shelter surface Ce sites for the formation of O_3. The applied scavengers exhibited similar effects in the degradation of solely OA and in the OA−ATZ combined system (Figure 9d and e). The addition of BrO_3^- slightly inhibited the PCO/Ce−CN system because it competed with O_3 for e_{cb}^-, thereby suppressing O_3 activation. TBA had a greater inhibitory effect on the PCO/Ce−CN system. When OA was solely degraded, the introduction of TBA reduced the OA removal from 89 to 24%. As for the OA−ATZ combined system, adding TBA decreased OA removal from 89 to 42%, verifying the non-negligible role of •OH in OA oxidation and the •OH-independent degradation pathways in the composite pollutant system. As exhibited in Figure S11 and Table S10, Ce−CN had a relatively large Lewis acid site (LAS), which indicated that LAS played a significant role in catalyzing O_3 in the PCO/Ce−CN system.[45] After the addition of PO_4^{3-}, the Lewis acid sites on the Ce−CN surface were masked, leading to suppression of O_3 activation. As a result, in both the OA-alone system and the OA−ATZ system, the pollutant removals were significantly inhibited. The introduction of DMSO exhibited the most pronounced inhibition on the PCO/Ce−CN system. In both the sole OA and OA−ATZ system, OA removals were almost inhibited. However, in the sole ATZ system (Figure 9f), the addition of DMSO reduced ATZ removal from 100 to 70%, which was approximately the same as TBA, while in the OA−ATZ system (Figure 9g), the addition of DMSO reduced ATZ removal to 40%. As a matter

https://doi.org/10.1021/acsami.5c09397
ACS Appl. Mater. Interfaces 2025, 17, 50650−50664

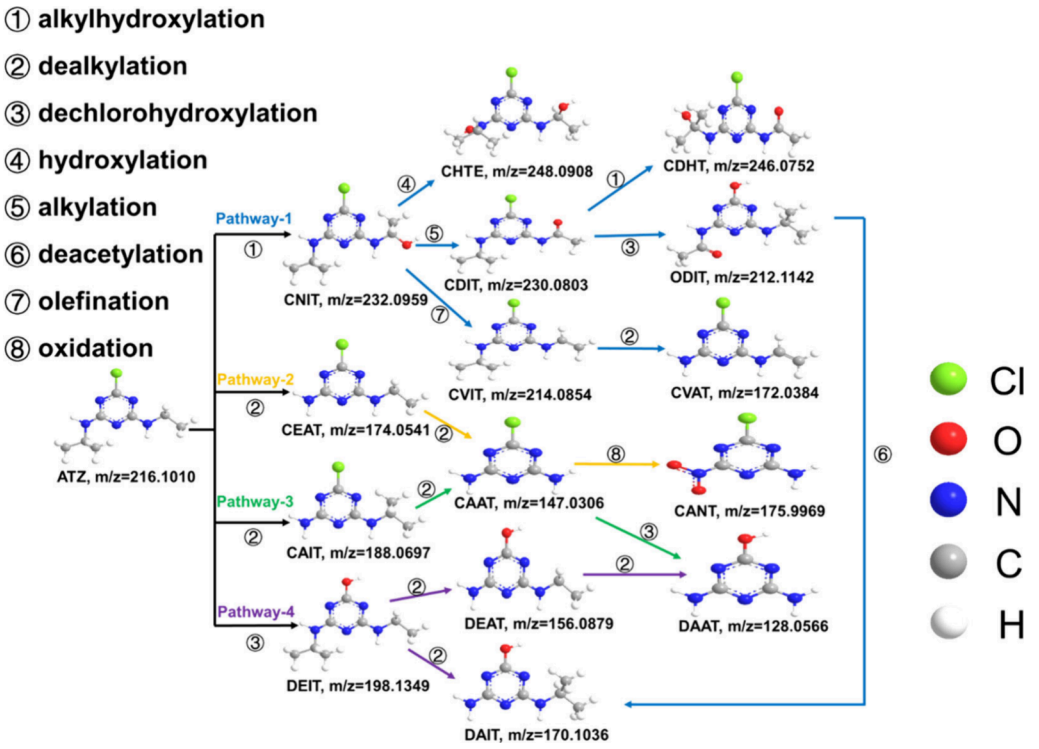

Figure 10. Degradation pathways of ATZ.

of fact, DMSO could not only quench surface-adsorbed active species but also had a high reaction rate with •OH.[46] Thus, in the sole ATZ system, ATZ removal was mainly governed by free •OH, while in the composite pollutant system, the degradation of OA and ATZ was primarily driven by •OH and surface-bound ROS.

In situ Raman spectroscopy was applied to observe the intermediate oxygen species formed on Ce−CN upon contact with ozone (Figure 9h). Characteristic peaks at 706 and 990 cm^{-1} were detected in the presence of O_3, corresponding to surface-adsorbed peroxide species ($*O_2$) and surface-adsorbed atomic oxygen (*O), respectively.[47] Overall, the results indicated that OA adsorbed onto the surface of Ce−CN, forming a Ce−OA complex that served as an active site for the adsorption of O_3 and subsequent decomposition of O_3 into *O and $*O_2$. *O, with an oxidation potential of 2.43 V, degraded pollutants by either directly attacking contaminants on the catalyst surface or protonating/reacting with O_3 to generate •OH, which indirectly oxidized contaminants.[48]

3.5. Degradation Pathways of ATZ. To elucidate the degradation pathways of ATZ, the transformation products in the PCO/Ce−CN/OA system were systematically analyzed by using LC−MS/MS. A total of 15 intermediates were identified, with their molecular structures were confirmed by MS/MS fragmentation patterns (Table S11). The primary reaction mechanisms included alkyl hydroxylation, dealkylation, dechlorohydroxylation, alkylation, deacetylation, hydroxylation, and olefination, consistent with previously reported literature.[49,50] As illustrated in Figure 10, four major degradation routes were identified. In pathway 1, hydroxylation of one or both alkyl side chains initially yielded CNIT and CHTE, where CNIT subsequently underwent alkylation to form CDIT. This intermediate was then further transformed via either alkyl hydroxylation to CDHT or dechlorohydroxylation to ODIT. Alternatively, CNIT could undergo olefination to produce CVIT, which then experienced dealkylation to form CVAT. Pathway 4 involved direct •OH attack, beginning with •OH substitution at the chlorine position to generate DEIT, followed by sequential dealkylation of both side chains to produce DEAT, DAIT, and DAAT. Notably, DAIT could also be formed through deacetylation of ODIT from pathway 1. Pathways 2 and 3 proceeded through stepwise dealkylation, where progressive removal of alkyl groups from both side chains formed CEAT, CAIT, and CAAT,[51] with CAAT being subsequently either oxidized to CANT or converted to DAAT via dechlorohydroxylation.

4. CONCLUSION

This study revealed the unique role of OA in Ce−CN-assisted photocatalytic ozonation for water treatment. Ce doping enhanced the light-harvesting ability, charge transfer rate, and $h_{vb}^{+}-e_{cb}^{-}$ separation efficiency of pure CN. Additionally, the incorporation of OA further reduced the bandgap and improved the electron transfer in Ce−CN, facilitating the degradation of both OA and coexisting ATZ. A similar trend was observed in the presence of other pollutants and in real water bodies. OA could be adsorbed on Ce−CN to form the Ce−OA complex. The strong electron-donating effect of OA promoted valence cycling of Ce(III)/Ce(IV), thereby enhancing the reactivity of Ce−CN with O_3. O_3 was decomposed into *O and •OH, which were the main ROS for pollutant degradation in the PCO/Ce−CN/OA process. This study provided novel insights into the role of metal-based catalysts in the PCO process, expanding the understanding of their underlying mechanisms.

■ ASSOCIATED CONTENT

Supporting Information

The Supporting Information is available free of charge at https://pubs.acs.org/doi/10.1021/acsami.5c09397.

https://doi.org/10.1021/acsami.5c09397
ACS Appl. Mater. Interfaces 2025, 17, 50650−50664

Test condition of EPR (Text S1), method for measuring the O_3 concentration (Text S2), preparation of the salt bridge (Text S3), instrument parameters of EPR (Table S1), test condition of HPLC (Table S2), S_{BET}, pore sizes, and pore volumes of CN and Ce−CN (Table S3), parameters of EXAFS fits for Ce−CN (Table S4), calculated bond lengths of Ce−CN (Table S5), water quality of the Guanzhou River (Table S6), first-order kinetic rate constant of light irradiation, heterogeneous catalytic ozonation, photocatalytic ozonation, and calculated synergy factor (Table S7), adsorption energy of tested carboxylic acids on Ce (Table S8), value of *a*, *b*, and *c* in different catalytic systems (Table S9), Lewis acidity of Ce−CN (Table S10), detected intermediates by LC−MS/MS (Table S11), N_2 adsorption−desorption isotherms and pore diameter distribution (inset) of catalysts (Figure S1), structural model of Ce−CN (Figure S2), ATZ removal in the single-pollutant system (Figure S3a), H_2O_2 production (Figure S3b), ATZ removal (Figure S3c) and OA removal in the dual-pollutant system by CN and Ce−CN (Figure S3d), OA removal in the dual-pollutant system with different OA concentrations (Figure S4), carboxylic acid produced in 15 min (Figure S5a), ATZ removal in the PCO/Ce−CN system (Figure S5b), 3DEEM spectra of (Figure S6a) before and (Figure S6b) after Ce−CN adsorption, ATR−FTIR spectra (Figure S6c), different coordination modes between carboxylic acids and the Ce active center (Figure S7), differential charge density map of OA on Ce (Figure S8), EIS plots (Figure S9a), photocurrent curves of CN and Ce−CN (Figure S9b and c), O_3 concentrations in different systems (Figure S10), and Py−FTIR spectra of Ce−CN (Figure S11) (PDF)

AUTHOR INFORMATION

Corresponding Authors

Weirui Chen − *Guangdong Key Laboratory of Environmental Catalysis and Health Risk Control, School of Environmental Science and Engineering, Institute of Environmental Health and Pollution Control, Guangdong University of Technology, Guangzhou, Guangdong 510006, China*; Email: wr_chen@gdut.edu.cn

Xingmei Guo − *School of Environment, South China Normal University, Key Laboratory of Theoretical Chemistry of Environment Ministry of Education, Guangdong Provincial Engineering Technology Research Center for Drinking Water Safety, Guangdong Provincial Key Lab of Functional Materials for Environmental Protection, Guangzhou, Guangdong 510006, China*; Email: 20081107@m.scnu.edu.cn

Laisheng Li − *School of Environment, South China Normal University, Key Laboratory of Theoretical Chemistry of Environment Ministry of Education, Guangdong Provincial Engineering Technology Research Center for Drinking Water Safety, Guangdong Provincial Key Lab of Functional Materials for Environmental Protection, Guangzhou, Guangdong 510006, China; School of Chemistry and Chemical Engineering, Key Laboratory of Clean Energy Materials Chemistry of Guangdong Higher Education Institutes, Lingnan Normal University, Zhanjiang, Guangdong 524048, China*; orcid.org/0000-0002-2091-4382; Phone: +86-20-39310185; Email: llsh@scnu.edu.cn; Fax: +86-20-39310187

Authors

Qi Chen − *School of Environment, South China Normal University, Key Laboratory of Theoretical Chemistry of Environment Ministry of Education, Guangdong Provincial Engineering Technology Research Center for Drinking Water Safety, Guangdong Provincial Key Lab of Functional Materials for Environmental Protection, Guangzhou, Guangdong 510006, China*

Jing Wang − *School of Environment, South China Normal University, Key Laboratory of Theoretical Chemistry of Environment Ministry of Education, Guangdong Provincial Engineering Technology Research Center for Drinking Water Safety, Guangdong Provincial Key Lab of Functional Materials for Environmental Protection, Guangzhou, Guangdong 510006, China*

Gaozu Liao − *School of Environment, South China Normal University, Key Laboratory of Theoretical Chemistry of Environment Ministry of Education, Guangdong Provincial Engineering Technology Research Center for Drinking Water Safety, Guangdong Provincial Key Lab of Functional Materials for Environmental Protection, Guangzhou, Guangdong 510006, China*

Xukai Li − *School of Environment, South China Normal University, Key Laboratory of Theoretical Chemistry of Environment Ministry of Education, Guangdong Provincial Engineering Technology Research Center for Drinking Water Safety, Guangdong Provincial Key Lab of Functional Materials for Environmental Protection, Guangzhou, Guangdong 510006, China*

Complete contact information is available at: https://pubs.acs.org/10.1021/acsami.5c09397

Notes

The authors declare no competing financial interest.

ACKNOWLEDGMENTS

This study was funded by the National Natural Science Foundation (52200016), the Guangdong Basic and Applied Basic Research Foundation (2024A1515011864), and the Guangzhou Basic and Applied Basic Research Foundation (2024A04J9934).

REFERENCES

(1) Chen, Y.-d.; Duan, X.; Zhou, X.; Wang, R.; Wang, S.; Ren, N.-q.; Ho, S.-H. Advanced oxidation processes for water disinfection: Features, mechanisms and prospects. *Chemical Engineering Journal* **2021**, *409*, 128207.

(2) Zhao, W.; Zeng, Y.; Zhao, Y.; Wu, X. Recent advances in metal-organic framework-based electrode materials for supercapacitors: A review. *Journal of Energy Storage* **2023**, *62*, 106934.

(3) Checa, M.; Figueredo, M.; Aguinaco, A.; Beltran, F. J. Graphene oxide/titania photocatalytic ozonation of primidone in a visible LED photoreactor. *Journal of Hazardous Materials* **2019**, *369*, 70−78.

(4) Lai, Z.; Yang, Y.; Yang, Z.; Ruan, W.; Yang, C.; Chen, Q.; Ding, K.; Zhang, J.; Hou, Y. Carbon nitride grafted with single-atom manganese and 2-hydroxy-4,6-di-methylpyrimidine: A visible-light-driven photocatalyst for enhanced ozonation of organic pollutants. *J. Colloid Interface Sci.* **2025**, *683*, 1106−1118.

(5) Xiao, J.; Xie, Y.; Cao, H.; Wang, Y.; Guo, Z.; Chen, Y. Towards effective design of active nanocarbon materials for integrating visible-light photocatalysis with ozonation. *Carbon* **2016**, *107*, 658−666.

(6) Tan, Y. S.; Chen, W. R.; Liao, G. Z.; Li, X. K.; Wang, J.; Wang, J. B.; Tang, Y. M.; Li, L. S. Role of metal-N-C electron transport channel within g-C_3N_4 for promoting water purification of photocatalytic ozonation. *Applied Catalysis B-Environment and Energy* **2024**, *351*, 124005.
(7) Mano, T.; Nishimoto, S.; Kameshima, Y.; Miyake, M. Water treatment efficacy of various metal oxide semiconductors for photocatalytic ozonation under UV and visible light irradiation. *Chemical Engineering Journal* **2015**, *264*, 221−229.
(8) Orge, C. A.; Faria, J. L.; Pereira, M. F. R. Photocatalytic ozonation of aniline with TiO_2-carbon composite materials. *Journal of Environmental Management* **2017**, *195*, 208−215.
(9) Mahmoodi, N. M. Photocatalytic ozonation of dyes using copper ferrite nanoparticle prepared by co-precipitation method. *Desalination* **2011**, *279* (1−3), 332−337.
(10) Liu, X.; Guo, Z.; Zhou, L.; Yang, J.; Cao, H.; Xiong, M.; Xie, Y.; Jia, G. Hierarchical biomimetic $BiVO_4$ for the treatment of pharmaceutical wastewater in visible-light photocatalytic ozonation. *Chemosphere* **2019**, *222*, 38−45.
(11) Farré, M. J.; Franch, M. I.; Malato, S.; Ayllón, J. A.; Peral, J.; Doménech, X. Degradation of some biorecalcitrant pesticides by homogeneous and heterogeneous photocatalytic ozonation. *Chemosphere* **2005**, *58* (8), 1127−1133.
(12) Cheng, X.; Liang, L.; Ye, J.; Li, N.; Yan, B.; Chen, G. Influence and mechanism of water matrices on H2O2-based Fenton-like oxidation processes: A review. *Sci. Total Environ.* **2023**, *888*, 164086.
(13) Chen, H.; Wang, J. Degradation and mineralization of ofloxacin by ozonation and peroxone (O_3/H_2O_2) process. *Chemosphere* **2021**, *269*, 128775.
(14) Tan, X.; Wang, S.; Ma, L.; Xue, W.; Dong, S.; Li, M.; Wang, P.; Wei, H.; Sun, C. Catalytic ozone oxidation of m-cresol by spirulina biochar-modified perovskite: Catalyst deactivation and in-situ regeneration. *Sep. Purif. Technol.* **2024**, *329*, 124994.
(15) Pu, Z.; Xiao, B.; Mao, S.; Sun, Y.; Ma, D.; Wang, H.; Zhou, J.; Cheng, Y.; Shi, J.-W. An electron-hole separation mechanism caused by the pseudo-gap formed at the interfacial Co-N bond between cobalt porphyrin metal organic framework and boron-doped g-C_3N_4 for boosting photocatalytic H_2 production. *J. Colloid Interface Sci.* **2022**, *628*, 477−487.
(16) Wei, W.; Han, X.; Shao, Y.; Xie, W.; Zhang, Y.; Yao, Y.; Zhao, W.; Han, R.; Li, S.; Zhang, Y.; Zheng, C. Comparing the effects of humic acid and oxalic acid on Pb(II) immobilization by a green synthesized nanocrystalline hydroxyapatite. *Chemosphere* **2021**, *285*, 131411.
(17) Sugihartono, V. E.; Mahasti, N. N. N.; Shih, Y.-J.; Huang, Y.-H. Photo-persulfate oxidation and mineralization of benzoic acid: Kinetics and optimization under UVC irradiation. *Chemosphere* **2022**, *296*, 133663.
(18) Zhang, F.; Tang, Y.; Yang, X.; Pan, Y.; Hou, Q.; Ding, Y.; Pei, J. Anti-lipid oxidation of chitosan oligosaccharide modified by laccase/TEMPO reaction. *Polymer* **2022**, *246*, 124742.
(19) Xie, Y.; Peng, S.; Feng, Y.; Wu, D. Enhanced mineralization of oxalate by highly active and Stable Ce(III)-Doped g-C_3N_4 catalyzed ozonation. *Chemosphere* **2020**, *239*, 124612.
(20) Wen, N.; Liu, J.; Qin, W.; Wang, X.; Zhu, C.; Zhou, D. Critical roles of low-molecular-weight organic acid in enhancing hydroxyl radical production by ferrous oxidation on γ-Al_2O_3 mineral surface. *Water Res.* **2024**, *261*, 122052.
(21) Cao, H. B.; Wang, J.; Kim, J. H.; Guo, Z.; Xiao, J. D.; Yang, J.; Chang, J. J.; Shi, Y. C.; Xie, Y. B. Different roles of Fe atoms and nanoparticles on g-C_3N_4 in regulating the reductive activation of ozone under visible light. *Appl. Catal., B* **2021**, *296*, 120362.
(22) Yang, F. C.; Jiang, G. D.; Yan, F.; Chang, Q. Fe/C magnetic nanocubes with enhanced peroxidase mimetic activity for colorimetric determination of hydrogen peroxide and glucose. *Microchimica Acta* **2019**, *186* (7), 417.
(23) Zhu, Z.; Ma, C. C.; Yu, K. S.; Lu, Z. Y.; Liu, Z.; Huo, P. W.; Tang, X.; Yan, Y. S. Synthesis Ce-doped biomass carbon-based g-C_3N_4 via plant growing guide and temperature-programmed technique for degrading 2-Mercaptobenzothiazole. *Appl. Catal., B* **2020**, *268*, 118432.
(24) Tan, Y.; Chen, W.; Liao, G.; Li, X.; Wang, J.; Tang, Y.; Li, L. Strategy for improving photocatalytic ozonation activity of g-C_3N_4 by halogen doping for water purification. *Appl. Catal., B* **2022**, *306*, 121133.
(25) Yuan, Z. X.; Tan, L.; Chen, W. R.; Wang, X.; Li, L. S.; Wang, J. Synergistic photocatalytic ozonation of eliminating chloramphenicol over a 2D MXene-derived heterojunction. *Chemical Engineering Journal* **2024**, *485*, 149857.
(26) Kwon, M.; Kye, H.; Jung, Y.; Yoon, Y.; Kang, J. W. Performance characterization and kinetic modeling of ozonation using a new method: R-OH,O_3 concept. *Water Res.* **2017**, *122*, 172−182.
(27) Zhang, J.; Shan, C.; Zhang, W.; Pan, B. In situ ligand-modulated activation of inert Ce(III/IV) into ozonation catalyst for efficient water treatment. *Proc. Natl. Acad. Sci. U.S.A.* **2023**, *120* (35), No. e2305255120.
(28) Zhu, J. N.; Zhu, X. Q.; Cheng, F. F.; Li, P.; Wang, F.; Xiao, Y. W.; Xiong, W. W. Preparing copper doped carbon nitride from melamine templated crystalline copper chloride for Fenton-like catalysis. *Appl. Catal., B* **2019**, *256*, 117830.
(29) Wang, J.; Xie, Y. B.; Yu, G. F.; Yin, L. C.; Xiao, J. D.; Wang, Y. X.; Lv, W. G.; Sun, Z.; Kim, J. H.; Cao, H. B. Manipulating Selectivity of Hydroxyl Radical Generation by Single- Atom Catalysts in Catalytic Ozonation: Surface or Solution. *Environ. Sci. Technol.* **2022**, *56* (24), 17753−17762.
(30) Yue, B.; Li, Q. Y.; Iwai, H.; Kako, T.; Ye, J. H. Hydrogen production using zinc-doped carbon nitride catalyst irradiated with visible light. *Sci. Technol. Adv. Mater.* **2011**, *12* (3), 034401.
(31) Li, X.; Zhu, W.; Lu, X.; Zuo, S.; Yao, C.; Ni, C. Integrated nanostructures of CeO_2/attapulgite/g-C_3N_4 as efficient catalyst for photocatalytic desulfurization: Mechanism, kinetics and influencing factors. *Chemical Engineering Journal* **2017**, *326*, 87−98.
(32) Su, L. N.; Wang, P. F.; Ma, X. L.; Wang, J. H.; Zhan, S. H. Regulating Local Electron Density of Iron Single Sites by Introducing Nitrogen Vacancies for Efficient Photo-Fenton Process. *Angew. Chem., Int. Ed.* **2021**, *60* (39), 21261−21266.
(33) Chen, F.; Liu, L.-L.; Wu, J.-H.; Rui, X.-H.; Chen, J.-J.; Yu, Y. Single-Atom Iron Anchored Tubular g-C_3N_4 Catalysts for Ultrafast Fenton-Like Reaction: Roles of High-Valency Iron-Oxo Species and Organic Radicals. *Adv. Mater.* **2022**, *34* (31), 2202891.
(34) Lai, C.; Yan, H. C.; Wang, D. B.; Liu, S. Y.; Zhou, X. R.; Li, X. P.; Zhang, M. M.; Li, L.; Fu, Y. K.; Xu, F. H.; Yang, X. F.; Huo, X. Q. Facile synthesis of Mn, Ce co-doped g-C_3N_4 composite for peroxymonosulfate activation towards organic contaminant degradation. *Chemosphere* **2022**, *293*, 133472.
(35) Mafa, P. J.; Malefane, M. E.; Idris, A. O.; Liu, D.; Gui, J. Z.; Mamba, B. B.; Kuvarega, A. T. Multi-elemental doped g-C_3N_4 with enhanced visible light photocatalytic Activity: Insight into naproxen Degradation, Kinetics, effect of Electrolytes, and mechanism. *Sep. Purif. Technol.* **2022**, *282*, 120089.
(36) Pines, D. S.; Reckhow, D. A. Effect of dissolved cobalt(II) on the ozonation of oxalic acid. *Environ. Sci. Technol.* **2002**, *36* (19), 4046−4051.
(37) Zhang, T.; Li, W. W.; Croué, J. P. Catalytic Ozonation of Oxalate with a Cerium Supported Palladium Oxide: An Efficient Degradation Not Relying on Hydroxyl Radical Oxidation. *Environ. Sci. Technol.* **2011**, *45* (21), 9339−9346.
(38) Zhou, J.; Chen, W.; Chen, Q.; Li, X.; Wang, J.; Liao, G.; Li, L. Construction of $BaTiO_3$/g-C_3N_4 heterojunction for promoting atrazine degradation of hydraulic-driven piezocatalytic ozonation. *Applied Catalysis B-Environment and Energy* **2025**, *362*, 124702.
(39) Awfa, D.; Ateia, M.; Fujii, M.; Yoshimura, C. Photocatalytic degradation of organic micropollutants: Inhibition mechanisms by different fractions of natural organic matter. *Water Res.* **2020**, *174*, 115643.
(40) Jacquin, C.; Lesage, G.; Traber, J.; Pronk, W.; Heran, M. Three-dimensional excitation and emission matrix fluorescence (3DEEM) for quick and pseudo-quantitative determination of protein- and

https://doi.org/10.1021/acsami.5c09397
ACS Appl. Mater. Interfaces 2025, 17, 50650−50664

humic-like substances in full-scale membrane bioreactor (MBR). *Water Res.* **2017**, *118*, 82−92.
(41) Shan, C.; Xu, Y.; Hua, M.; Gu, M.; Yang, Z.; Wang, P.; Lu, Z.; Zhang, W.; Pan, B. Mesoporous Ce-Ti-Zr ternary oxide millispheres for efficient catalytic ozonation in bubble column. *Chemical Engineering Journal* **2018**, *338*, 261−270.
(42) Yan, H.; Lu, P.; Pan, Z.; Wang, X.; Zhang, Q.; Li, L. Ce/SBA-15 as a heterogeneous ozonation catalyst for efficient mineralization of dimethyl phthalate. *J. Mol. Catal. A: Chem.* **2013**, *377*, 57−64.
(43) Chen, L.; Dong, X.; Feng, R.; Li, W.; Ding, D.; Cai, T.; Jiang, C. Oxalic acid enhanced ferrous/persulfate process for the degradation of triclosan in soil: Efficiency, mechanism and a column study. *Chemical Engineering Journal* **2023**, *473*, 144961.
(44) Gu, H.; Lan, J.; Hu, H.; Jia, F.; Ai, Z.; Zhang, L.; Liu, X. Surface oxygen vacancy-dependent molecular oxygen activation for propane combustion over a -MnO_2. *Journal of Hazardous Materials* **2023**, *460*, 132499.
(45) Yu, D.; Wang, L.; Yang, T.; Yang, G.; Wang, D.; Ni, H.; Wu, M. Tuning Lewis acidity of iron-based metal-organic frameworks for enhanced catalytic ozonation. *Chemical Engineering Journal* **2021**, *404*, 127075.
(46) Yu, G. F.; Wang, Y. X.; Cao, H. B.; Zhao, H.; Xie, Y. B. Reactive Oxygen Species and Catalytic Active Sites in Heterogeneous Catalytic Ozonation for Water Purification. *Environ. Sci. Technol.* **2020**, *54* (10), 5931−5946.
(47) Cheng, Y. Z.; Wang, B. Y.; Yan, P. W.; Shen, J. M.; Kang, J.; Zhao, S. X.; Zhu, X. W.; Shen, L. L.; Wang, S. Y.; Shen, Y.; Chen, Z. L. In-situ formation of surface reactive oxygen species on defective sites over N-doped biochar in catalytic ozonation. *Chemical Engineering Journal* **2023**, *454*, 140232.
(48) Wang, Y.; Chen, L.; Chen, C.; Xi, J.; Cao, H.; Duan, X.; Xie, Y.; Song, W.; Wang, S. Occurrence of both hydroxyl radical and surface oxidation pathways in N-doped layered nanocarbons for aqueous catalytic ozonation. *Applied Catalysis B: Environmental* **2019**, *254*, 283−291.
(49) Zhu, S.; Dong, B.; Yu, Y.; Bu, L.; Deng, J.; Zhou, S. Heterogeneous catalysis of ozone using ordered mesoporous Fe_3O_4 for degradation of atrazine. *Chemical Engineering Journal* **2017**, *328*, 527−535.
(50) Li, J.; Wan, Y.; Li, Y.; Yao, G.; Lai, B. Surface Fe(III)/Fe(II) cycle promoted the degradation of atrazine by peroxymonosulfate activation in the presence of hydroxylamine. *Appl. Catal., B* **2019**, *256*, 117782.
(51) Ye, G.; Luo, P.; Zhao, Y.; Qiu, G.; Hu, Y.; Preis, S.; Wei, C. Three-dimensional Co/Ni bimetallic organic frameworks for high-efficient catalytic ozonation of atrazine: Mechanism, effect parameters, and degradation pathways analysis. *Chemosphere* **2020**, *253*, 126767.

https://doi.org/10.1021/acsami.5c09397
ACS Appl. Mater. Interfaces 2025, 17, 50650−50664